AGU100 ADVANCING EARTH AND SPACE SCIENCE

JGR Oceans

RESEARCH ARTICLE

10.1029/2018JC014451

Surface Water Temperature Heterogeneity at Subpixel Satellite Scales and Its Effect on the Surface Cooling Estimates of a Large Lake: Airborne Remote Sensing Results From Lake Geneva

Abolfazl Irani Rahaghi[1], **Ulrich Lemmin**[1], **and David Andrew Barry**[1]

[1]Ecological Engineering Laboratory (ECOL), Environmental Engineering Institute, Faculty of Architecture, Civil and Environmental Engineering (ENAC), Ecole Polytechnique Fédérale de Lausanne (EPFL), Lausanne, Switzerland

Key Points:

- Airborne surface water temperature heterogeneity patterns on a lake resolved at subpixel satellite scale (1-m resolution) are presented
- The surface cooling distribution can be different from the surface water temperature distribution under predominantly stable conditions
- The surface water temperature heterogeneity influences the area-averaged surface cooling estimates under near-neutral conditions

Supporting Information:

- Supporting Information S1

Correspondence to:
A. Irani Rahaghi,
abolfazl.iranirahaghi@epfl.ch

Citation:
Irani Rahaghi, A., Lemmin, U., & Barry, D. A. (2019). Surface water temperature heterogeneity at subpixel satellite scales and its effect on the surface cooling estimates of a large lake: Airborne remote sensing results from Lake Geneva. *Journal of Geophysical Research: Oceans*, *124*. https://doi.org/10.1029/2018JC014451

Received 7 AUG 2018
Accepted 29 DEC 2018
Accepted article online 5 JAN 2019

Abstract The dynamics of spatial heterogeneity of lake surface water temperature (LSWT) at subpixel satellite scale O(1 m) and its effect on the surface cooling estimation at typical satellite pixel areas O(1 km^2) were investigated using an airborne platform. The measurements provide maps that revealed spatial LSWT variability with unprecedented detail. The cold season data did not show significant LSWT heterogeneity and hence no surface cooling spatial variability. However, based on three selected daytime subpixel-scale maps, LSWT patterns showed a variability of >2 °C in the spring and >3.5 °C in the summer, corresponding to a spatial surface cooling range of >20 and >40 W/m^2, respectively. Due to the nonlinear relationship between turbulent surface heat fluxes and LSWT, negatively skewed LSWT distributions resulted in negatively skewed surface cooling patterns under very stable or predominantly unstable atmospheric boundary layer (ABL) conditions and positively skewed surface cooling patterns under predominantly stable ABL conditions. Implementing a mean spatial filter, the effect of area-averaged LSWT on the surface cooling estimation up to a typical satellite pixel was assessed. The effect of the averaging filter size on the mean spatial surface cooling values was negligible, except for predominantly stable ABL conditions. In that situation, a reduction of ~3.5 W/m^2 was obtained when moving from high O(1 m) to low O(1 km) pixel resolution.

Plain Language Summary Lake surface water temperature (LSWT) is one of the main parameters required for estimating surface cooling at the air-water interface and is also essential for understanding other processes (such as ecosystem dynamics, climate change, and numerical weather prediction) in lakes. Usually, surface cooling is determined from in situ point measurements or satellite images. Satellite thermal images resolve surface areas with a typical pixel resolution of O(1 km). Therefore, satellite data can depict large-scale thermal patterns. But can LSWT spatial variability be significant at subpixel satellite resolution over a large lake? What is the effect of such variability on area-averaged surface cooling estimates? To address these questions, a measurement system, including a balloon-launched airborne platform for thermography and a catamaran for in situ measurements along predefined tracks, was used for LSWT mapping and calibration. Surface cooling patterns were then estimated using a calibrated bulk model. Results showed insignificant LSWT heterogeneity and hence no surface cooling spatial variability during the cold seasons. However, a notable spatial variability of >2 °C and > 3.5 °C was found in spring and summer, respectively. The effect of LSWT heterogeneity on surface cooling variability was significant, in particular, when air-water temperature differences were close to 0.

1. Introduction

Lake surface water temperature (LSWT) is an important parameter for characterizing many different aspects of lake dynamics. Resolving the spatiotemporal variability of LSWT, particularly on smaller scales, is essential in order to advance in the understanding and quantification of a wide range of processes in lakes, such as ecosystem dynamics (Bauersachs et al., 2015; Beaulieu et al., 2013; Binding et al., 2018; Bonvin et al., 2013), climate change, and numerical weather prediction (Balsamo et al., 2012; Le Moigne et al., 2016). LSWT is considered a fundamental variable in climate change investigations. Many studies reported on LSWT warming over the past decades and some of them showed that LSWT is even warming faster than air temperatures (e.g., Adrian et al., 2009; Arvola et al., 2010; Austin & Colman, 2007). However, a high level of spatial

heterogeneity in LSWT warming rates (or cooling rates in some cases) was reported in regional (e.g., Austin & Colman, 2007; Lemmin & Amouroux, 2013) and in global studies (O'Reilly et al., 2015). Woolway and Merchant (2018) recently demonstrated that within-lake variations of LSWT warming trends can also be expected. Since LSWT is the key coupling parameter at the interface of the atmospheric boundary layer (ABL) and the lake surface layer, its spatiotemporal variability influences surface cooling estimates at this interface.

Long-wave radiation and surface turbulent heat fluxes that are controlled by LSWT are the major cooling components of air-water heat exchange in lakes during ice-free periods (e.g., Van Emmerik et al., 2013; Xue et al., 2015), even though other factors, for example, accelerated snow melt (e.g., G. Q. Zhang et al., 2014), could affect LSWT and indirectly influence the surface cooling. Surface cooling estimates can be sensitive to the space and time resolution of input variables such as LSWT (Gulev, 1997; Hughes et al., 2012). A small (~1 °C) variation in LSWT, particularly under near-neutral ABL stability conditions, can result in a significant modification of the surface cooling of a water body (Brodeau et al., 2017; Mahrt & Hristov, 2017; Mahrt & Khelif, 2010).

To estimate LSWT and surface heat fluxes over inland water bodies, in situ point measurements (e.g., Assouline et al., 2008; Nordbo et al., 2011; Spence et al., 2011; Van Emmerik et al., 2013) or satellite surface temperature data (e.g., Alcantara et al., 2010; Lofgren & Zhu, 2000; Moukomla & Blanken, 2017) are often used. Satellite thermal images are representative for a surface area with typical pixel resolution of O(1 km). Therefore, satellite data can only resolve large-scale thermal patterns (e.g., Oesch et al., 2008; Pareeth et al., 2017; Sima et al., 2013), but not subpixel processes. Hereinafter, subpixel scale refers to horizontal structures ranging from O(1 m) to O(100 m). Past studies have examined subpixel-scale surface temperature variability by using airborne systems. However, due to the challenges intrinsic to thermal image registration over water (Rahaghi et al., 2019) or instrumental restrictions, they only reported along-track point (Mahrt & Khelif, 2010) or area-averaged (Castro et al., 2017) measurements. These studies observed skin temperature variations of >1 °C within ~1-km distance, which can affect the area-averaged surface heat flux calculation. Other studies employed infrared thermography to investigate small-scale (less than 1-m pixel resolution) surface water and heat flux horizontal variability (Garbe et al., 2004, 2003; Handler & Smith, 2011; Marruedo Arricibita et al., 2018; Schnieders et al., 2013; Veron et al., 2008).

Due to LSWT heterogeneity, air-water temperature differences and consequently the ABL stability conditions can be spatially variable at subpixel scales. The turbulent cooling response to the LSWT distribution is also affected by the spatial heterogeneity of surface stress. Turbulent heat fluxes are found to be more sensitive to skin temperature under near-neutral ABL stability conditions (Mahrt & Hristov, 2017; Mahrt & Khelif, 2010). Therefore, bulk algorithms that take into account ABL stability were preferred for this study. The surface stress and turbulent heat flux coefficients are coupled by the Monin-Obukhov similarity theory (Monin & Obukhov, 1954) with some parameterizations (e.g., Fairall et al., 2003; Woolway et al., 2015; Zeng et al., 1998) or through bulk Richardson number concepts (Mahrt & Hristov, 2017; Mahrt & Khelif, 2010).

In the present case study, we constructed maps of LSWT subpixel satellite scale variability. A measurement system, including an airborne platform for thermography and a catamaran for in situ ground truthing, was used for LSWT mapping and calibration. Several field campaigns were carried out over Lake Geneva, the largest lake in western Europe. Four daytime (afternoon) missions covering different ABL stability conditions were selected for the present study. The effect of LSWT variability on the surface cooling distribution and its area-averaged estimate was assessed without resolving the spatial variability of other meteorological parameters. In order to support the feasibility of this assumption, a sensitivity analysis on the range of meteorological parameters is presented, using the same along-track measurements of LSWT and air temperature variability measured by the catamaran.

2. Materials and Methods

2.1. Lake Surface Cooling Formulas

The equation for cooling from a lake surface Q_c contains a long-wave radiative term Q_{br} and two turbulent components, latent (evaporation, Q_{ev}) and sensible (convection, Q_{co}) heat fluxes:

$$Q_c = Q_{br} + Q_{ev} + Q_{co} \tag{1}$$

All the heat flux terms were assumed positive upward (out of the lake). Table 1 summarizes the formulas used for estimating the surface cooling components in the right-hand side of equation 1. Back radiation, Q_{br}, was modeled with the Stefan-Boltzmann law (equation 2, Table 1). Following studies at other sites (e.g., Davies et al., 1971; Woolway et al., 2018), we applied a constant water surface emissivity of 0.97. Based on satellite LSWT data and meteorological parameters from a numerical model calibrated at two locations on Lake Geneva, the Monin-Obukhov similarity theory (Monin & Obukhov, 1954) was found to provide the best estimates of turbulent heat fluxes over this lake (Rahaghi et al., 2018). We applied this calibrated model to the subpixel-scale short-term data presented here (section 2.2). A set of coupled equations (equations 3e, Table 1) had to be solved iteratively to obtain the drag, humidity, and temperature bulk transfer coefficients, that is, C_d, C_e, and C_h, respectively, in order to calculate the turbulent surface heat fluxes, Q_{ev} and Q_{co}. The details of these equations, their solution procedure, and their calibration can be found elsewhere (Rahaghi et al., 2018; Woolway et al., 2015; Zeng et al., 1998).

For f_m, f_e, and f_h (Table 1), which are required to resolve Q_{ev} and Q_{co}, we employed empirical expressions that are mainly used over other inland water bodies (e.g., Woolway et al., 2015; Zeng et al., 1998):

$$f_m(\zeta) = \begin{cases} 5+\zeta & \zeta>1 \quad \text{(very stable)} \\ 1+5\zeta & 0\le\zeta\le1 \quad \text{(stable)} \\ (1-16\zeta)^{-1/4} & -1.574\le\zeta<0 \quad \text{(unstable)} \\ (0.7\kappa^{2/3})(-\zeta)^{1/3} & \zeta<-1.574 \quad \text{(very unstable)} \end{cases} \tag{4a}$$

$$f_e(\zeta) = f_h(\zeta) = \begin{cases} 5+\zeta & \zeta>1 \quad \text{(very stable)} \\ 1+5\zeta & 0\le\zeta\le1 \quad \text{(stable)} \\ (1-16\zeta)^{-1/2} & -0.465\le\zeta<0 \quad \text{(unstable)} \\ (0.9\kappa^{4/3})(-\zeta)^{-1/3} & \zeta<-0.465 \quad \text{(very unstable)} \end{cases} \tag{4b}$$

The relationship between LSWT (T_w) and the surface cooling terms, Q_{br} (equation 2, Table 1), Q_{ev} and Q_{co} (equations 3a–3e, Table 1), is nonlinear, in particular, for the turbulent heat fluxes. Therefore, the response of surface cooling formulas to the LSWT distribution is expected to be nonlinear. This might affect area-averaged surface cooling estimates.

2.2. Data Set and Study Site

A two-platform measurement system composed of (i) a thermal imagery package suspended from a balloon (called BLIMP) and (ii) an autonomously operating catamaran (called ZiviCat) for in situ measurements was used to obtain LSWT maps resolved at subpixel scales.

The balloon (typically placed between 300 and 800 m above the lake) was tethered to a winch on a boat that accompanied ZiviCat, rather than ZiviCat itself. Even though ZiviCat includes obstacle-detection capabilities (Paccaud & Barry, 2018), it is legally mandated to be used under direct observation from another boat. The balloon carried a thermal imagery package (Liardon & Barry, 2017) suspended beneath it. The package included a *FLIR Tau2 LWIR* camera (640 × 512 pixel resolution, 14-bit digital output) and a *RGB Raspberry Pi* camera (used for visual inspection and verification), as well as equipment for its position (GPS), orientation, tilt angles (inertial measurement unit), height, and communication with the boat. Unlike other aerial systems such as aircraft or drones, the BLIMP system is less affected by vibration and tilting, as we confirmed by comparing BLIMP images with those obtained with a custom-made autonomous drone (Liardon et al., 2017).

The thermal images were registered and were calibrated implementing an image processing procedure to create the final LSWT maps with subpixel-scale resolution. In this procedure, a pixelwise two-point linear correction and a probability density function (PDF) matching in regions of overlap between sequential images were used for nonuniformity (spatial noise) and drift (temporal noise) corrections, respectively. A feature matching-based algorithm, combining blob and region detectors, was implemented to create composite thermal images, and a mean value of the overlapped images at each location was considered as a

Table 1
Bulk Formulas Used to Calculate Back Long-Wave Radiation (Using Stefan-Boltzmann Law) and Sensible and Latent Surface Heat Fluxes (Using Monin-Obukhov Similarity Theory)

Formula		Equation
$Q_{br} = 0.972\sigma(T_w + 273.15)^4$		(2)
$Q_{ev} = C_e\rho_z L_v u_z(q_s - q_z) = \rho_z L_v u_* q_*$, $Q_{co} = \rho_z C_{p,\,a} C_h u_z(T_w - T_z) = \rho_z C_{p,\,a} u_* T_*$		(3a)
$\tau = C_d\rho_z u_z^2 = \rho_z u_*^2$		(3b)
$f_m(\zeta) = (\kappa z_u/u_*)(\partial u/\partial z)$, $f_e(\zeta) = (\kappa z_q/q_*)(\partial q/\partial z)$, $f_h(\zeta) = (\kappa z_t/T_*)(\partial T/\partial z)$		(3c)
$\zeta = zL_w^{-1} = -\kappa z g\left[Q_{co}/C_{p,a} + 0.61\left(\widehat{T}_z Q_{ev}/L_v\right)\right]/\left[\rho_z u_*^3 \widehat{T}_z(1 + 0.61 q_z)\right]$		(3d)
$z_0 = 0.013u_*^2/g + 0.01\nu_a/u_*$, $z_{0q} = z_{0t} = z_0 \exp\left[-1.52(u_* z_0/\nu_a)^{0.25} + 2.57\right]$		(3e)
Symbols		Value
$C_e/C_d/C_h$	Humidity/momentum/temperature bulk transfer coefficients	—
$C_{p,a}$	Specific heat capacity of air at constant pressure (J·kg^{-1}·K^{-1})	1,004
e_s	Saturated water vapor pressure (hPa)	$e_s = 6.112 \exp[17.62T_w/(T_w + 243.12)]$
$f_e/f_h/f_m$	Flux gradient relations for humidity/temperature/momentum	Equation 3c
g	Gravitational acceleration (m/s^2)	9.81
L_v	Latent heat of vaporization (J/kg)	$L_v = 2.5 \times 10^6 - 2.3 \times 10^3 T_w$
L_w	Monin-Obukhov length	—
P_{atm}	Air pressure (hPa)	—
q_a	Air specific humidity (kg/kg dry air)	$q_a = 0.62e_a/(P_{\text{atm}} - 0.38e_a)$
q_s	Saturated specific humidity (kg/kg dry air)	$q_s = 0.62e_s/(P_{\text{atm}} - 0.38e_s)$
$q_z/\widehat{T}_z/u_z$	Specific humidity/absolute temperature/wind speed at height z	—
q_*/T_*	Scaling humidity/temperature	—
T_w	Lake surface water temperature (°C)	—
u_*	Air friction velocity (m/s)	—
$z_q/z_t/z_u$	Height of humidity/temperature/wind speed data (m)	—
$z_0/z_{0q}/z_{0t}$	Roughness length of momentum/humidity/temperature (m)	Equation 3e
κ	Von Karman constant	0.41
υ_a	Air viscosity (m^2/s)	1.6×10^{-5}
ρ_z	Air density at height z (kg/m)	$\rho_z = 100[(P_{\text{atm}} - e_z)/287.1 + e_z/461.5]/\widehat{T}_z$
σ	Stefan-Boltzmann constant (W·m^{-2}·K^{-4})	5.67×10^{-8}
τ	Air-water momentum flux (N/m^2)	Equation 3b
ζ	ABL stability parameter	Equation 3d

representative value of that pixel. Finally, the measured in situ temperatures measured by ZiviCat were used for the radiometric calibration. Details are given in Rahaghi et al. (2019).

Simultaneous ground truthing of the BLIMP data was achieved using the ZiviCat. It can measure in situ near-surface (down to 1.5 m) water temperatures using 10 RBRsolo thermistors (resolution: 0.002 °C, 2 Hz; RBR, last accessed on 18 October 2018), as well as lake current profiles, radiative heat flux, wind speed (*S11100H Ammonit*; measurement height ~2 m above the water surface; accuracy: 1% of measured value or <0.2 m/s, 2 Hz), air temperature (*SBE* 56 thermistor; measurement height ~0.6 m above the water surface; accuracy: 0.002 °C, 1 Hz), and relative humidity (083E-L Campbell-Scientific; measurement height ~2.1 m above the water surface; accuracy: 2%, 1 Hz). The shielded air temperature sensor was mounted at a height of 60 cm above the water in front of the catamaran on a mast together with the water temperature sensors. Some of these sensors, however, were not available for some of the field measurements. ZiviCat moves at a speed of ~1 m/s and has additional instruments and equipment for the position (GPS), stability (inertial measurement unit), data recording, and communication. This allows for real-time data control, correction, and analysis on the boat that accompanies ZiviCat and on which the winch for BLIMP is mounted. Details of the systems and sensors are presented in Barry et al. (2019). It should be noted that the whole measurement platform was continuously moving during the missions to cover the surface area along a predetermined trajectory. The ZiviCat platform was designed and equipped to measure the along-track data but could not determine spatial meteorological maps. Furthermore, the current ZiviCat configuration does not allow resolving the ABL at fine spatial and temporal scales, due to the long response time of the airside thermistor and humidity sensors, turbulence generated by the sensor shielding, and the continuous ZiviCat motion.

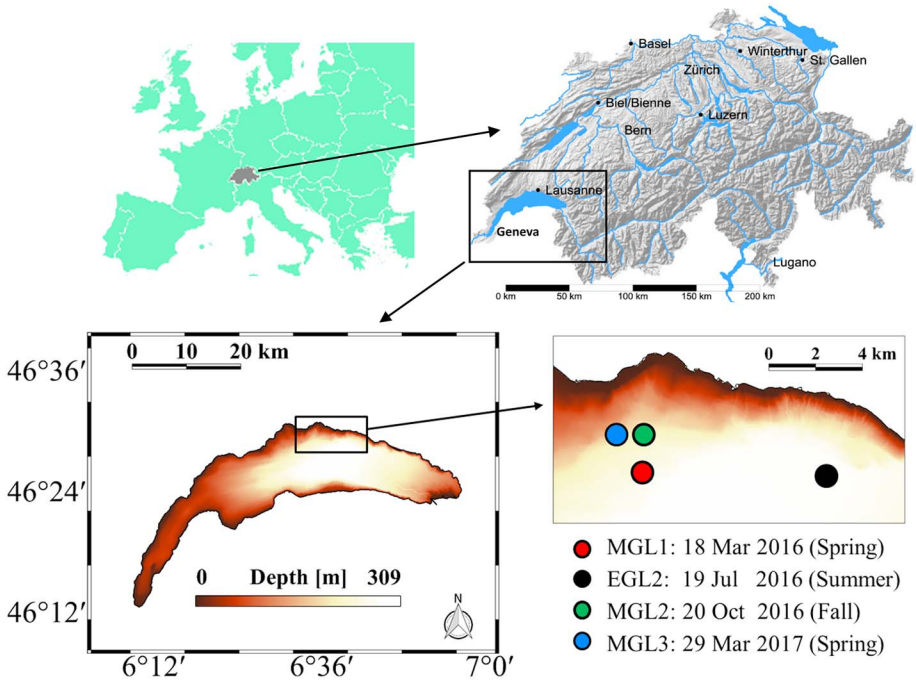

Figure 1. Location and bathymetry (see legend in bottom left panel) of Lake Geneva. The inset (bottom right panel) shows the area where the four selected missions, MGL1, EGL2, MGL2, and MGL3, were carried out. The date/season of each field mission is indicated in the bottom right legend.

Although a fine-scale study may provide more details on the air-water exchange processes, we emphasize that here we address processes at subpixel scales.

This study was carried out on Lake Geneva (Local name: *Lac Léman*). Located between Switzerland and France, it is a large, deep, crescent-shaped perialpine lake with a mean surface altitude of 372 m (Figure 1). It is approximately 70 km long, with a maximum width of 14 km, a surface area of 582 km^2, a volume of 89 km^3, and a maximum depth of 309 m.

Four field measurement data sets, MGL1, EGL2, MGL2, and MGL3 (Figure 1 and Table 2), were selected for this study. The field measurements were performed during the daytime and over predefined areas on the lake. To avoid the effect of coastal mixing on the temporal and spatial patterns of LSWT, we present the results for deep areas sufficiently far from the shores. All the measurements were taken under weak wind conditions (less than ~2 m/s) when LSWT spatial patterns are more likely to occur, and data are less contaminated by surface waves and BLIMP lateral movements. A mission usually takes ~5–6 hr, but to minimize the effect of mean LSWT temporal variation on the presented results, ~25 to 30 min segments of each data set were selected. The presented data are typical of the observed subpixel LSWT variability, except for MGL2. On that date, there were insufficient features for an image analysis, due to very small temporal and spatial variations of LSWT, and thus, only ~7 min of the data were analyzed. The calibration of the MGL2 thermal images was based on the minimum and maximum values. For the other three missions, we used the ZiviCat continuous temperature data for the calibration of the BLIMP registered image (Rahaghi et al., 2019). As will be discussed in section 3, the different calibration procedure for the MGL2 mission did not affect the findings of this study.

Meteorological data are also required for the surface cooling estimation (equations 2 to (4a) and (4b)). Due to equipment limitations, spatial maps of these data corresponding to the LSWT maps could not be resolved in this study. However, as will be shown below, we did not find a significant correlation between the near-surface temperature dynamics and the meteorological along-track data measured by the ZiviCat. Furthermore, the standard deviations of the measured data during the relatively short duration of the selected segments were on average small, except for air temperature during the MGL3 mission, performed under intense springtime radiative forcing (Table 2). Therefore, the heat flux calculations were based on

Table 2
Time, Number of Frames, Pixel Resolution, and Meteorological Parameters (U_{10}: Wind Speed, T_a: Air Temperature, and ϕ_{rel}: Relative Humidity) of the Four Selected Field Missions Used in This Study (See Figure 1 for Locations and Dates)

Field mission	Time	Number of frames	Pixel resolution (m)	U_{10} (m/s)	T_a (°C)	ϕ_{rel} (%)
MGL1	~15 hr30	287	0.8	0.6	9.8	60.1
EGL2	~17 hr30	496	0.8	1.3 (0.2)	25.2 (0.27)	60.1 (3.1)
MGL2	~14 hr00	81	2.7	2 (0.5)	12.3 (0.15)	50.1 (1.2)
MGL3	~13 hr40	315	1.4	2	13.5 (0.96)	66.7

Note. The standard deviations of the ZiviCat meteorological measurements are indicated in parentheses.

the average values of the meteorological data. A sensitivity analysis is presented in section 3.4 to quantify the uncertainty associated with this assumption. Some meteorological data were not recorded during the MGL1 and MGL3 missions. In those cases, we used the assimilated results of a numerical weather model (COSMO, last accessed on 18 July 2018) for the wind speed (at 10 m) and relative humidity (at 2 m) for the MGL1 and MGL3 missions, and the air temperature (at 2 m) of MGL1 (Table 2). The feasibility of using over lake COSMO data was previously demonstrated (Cimatoribus et al., 2018; Rahaghi et al., 2018). For a better comparison in Table 2, the averaged wind speed values measured by the ZiviCat (at ~1.8 m) were converted to the wind speed at 10 m, U_{10}, assuming a power law profile (Hsu et al., 1994):

$$U_{10} = u_z(10/z)^{0.11} \tag{5}$$

It should be noted, however, that the data at the measurement height were used for the surface cooling estimations.

3. Results and Discussion

3.1. Spatial Variability of LSWT at Subpixel Scales

LSWT maps produced from the calibrated thermal images (Rahaghi et al., 2019) for the selected missions are presented in Figure 2. The number of frames used to create each of these composite maps is given in Table 2. The BLIMP irradiance values and the corresponding ZiviCat near-surface temperatures have a correlation coefficient of >89% and a root-mean-square difference of <0.17 °C (Figure S1 in the supporting information, SI). The PDF for each LSWT map is also given in the bottom panels of Figure 2.

Various subpixel-scale cold-warm patches and streak-like structures over the lake surface area are evident in all maps. This suggests that the subpixel-scale LSWT spatial variability within a typical satellite pixel can be significant (comparable with the basin-scale variation). The spatial variability is more pronounced during the MGL1 (Figure 2a) and EGL2 (Figure 2b) missions with LSWT spatial ranges of >2 and >3.5 °C, respectively, over an area covering less than 1 km^2. MGL2 (Figure 2c) is a representative case for the cold season from October to February, when the spatial variability of LSWT at subpixel scales is negligible (<0.1 °C; smaller than the accuracy of remote sensing measurements). The observed LSWT patchiness over the total measured tracks (not shown here) was spatially and temporally variable throughout the day. For example, the springtime LSWT spatial variability was found not to be significant before 13 hr00 compared to the late afternoon data as was shown here. For this study, we only selected segments of the data with significant LSWT heterogeneity.

Except for MGL2 (Figure 2c), when the temperature in the uppermost layer of the water column was fairly uniform and the spatial variability was negligible, the remaining selected LSWT patterns show a negatively skewed distribution (skewness values of −0.8, −0.4, and −0.7 for MGL1, EGL2, and MGL3, respectively). Determining the reason for such skewness is beyond the scope of this paper. However, previous studies have examined the surface temperature distribution at small scales in the field (Veron et al., 2008) or under controlled laboratory conditions (Garbe et al., 2004; Handler & Smith, 2011) and found that the skewness of temperature field varies with the wind speed, that is, it is positive at low wind speeds and negative for wind speeds >2 m/s. Handler and Smith (2011) attributed the negative skewness of the surface water temperature distribution to elongated cold bands. Such cold bands were also observed in our LSWT patterns, as is

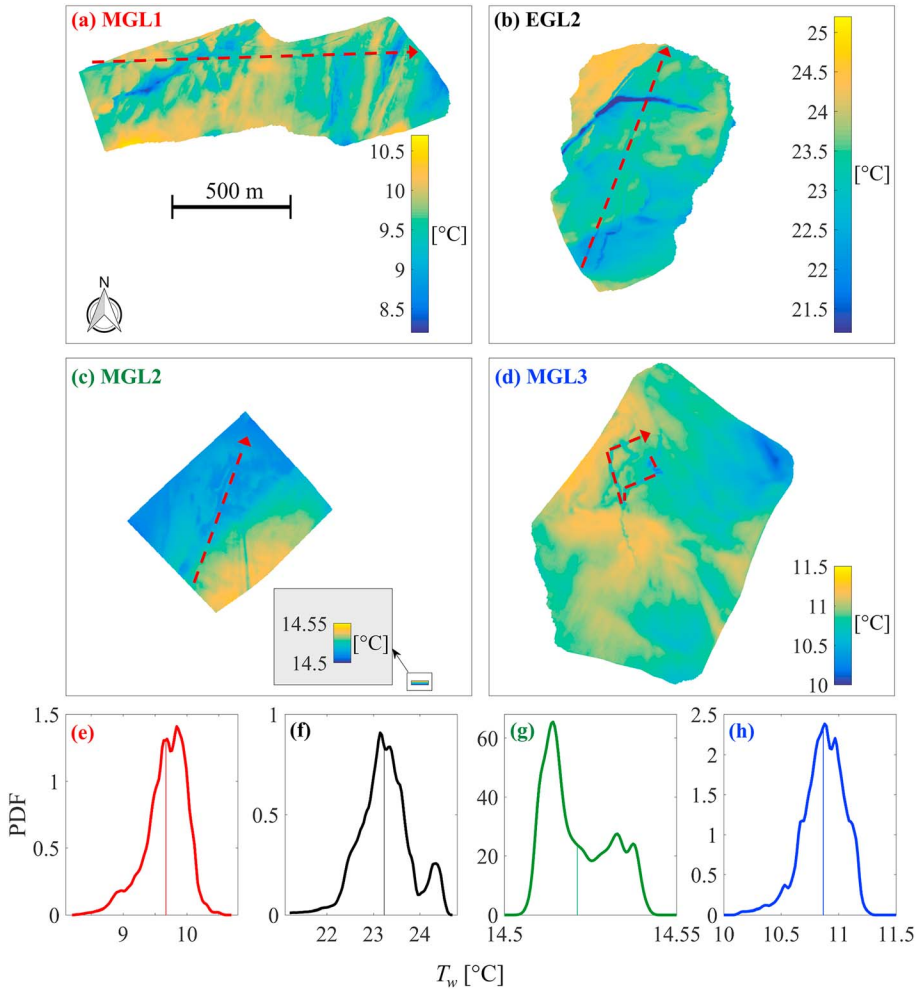

Figure 2. Subpixel satellite scale lake surface water temperature (LSWT) maps for the four selected field missions: (a) MGL1, (b) EGL2, (c) MGL2, and (d) MGL3 and their corresponding probability distribution function (PDF) curves (e) MGL1, (f) EGL2, (g) MGL2, and (h) MGL3. For the location and the date/season of each panel see Figure 1. In each of the four LSWT maps, a red dashed line marks the track of the ZiviCat and the arrowhead at the end of the line indicates the direction of motion. In order to be able to compare the different missions, all temperature maps have been placed into panels of identical size (approximately 1.4-km × 1.4-km area; ~2 typical satellite pixels) and all temperature legends use the same per degrees Celsius scale. This results in different legend lengths. Note that in (c) this temperature scaling is given in the small inset with an arrow indicating the zoomed color bar for easier reading. The axis scales of the PDF plots are also different in each panel, and the thin vertical lines in (e) to (h) indicate the mean value for each curve.

particularly evident in Figure 2a, even though our measurements were taken under weak surface wind speeds (<2 m/s).

In order to gain further insight into the dynamics of LSWT and ABL stability, the LSWT and air temperature data recorded by the ZiviCat along the tracks in the different missions are shown in Figure 3; no air temperature data are available for mission MGL1. Different dynamics can be seen between the summer and the fall/spring missions. In the summer (EGL2), the LSWT record is characterized by strong high-frequency variability with amplitudes of tenths of a degree that are only marginally visible in the aerial LSWT maps and are at the temporal limit of resolution of the instruments. Air temperature is initially slightly below LSWT indicating a potentially unstable ABL but is above the water temperature for the rest of the mission. In the fall (MGL2), the ABL is unstable with air temperatures well below those of the water. LSWT variability is very small. In the spring (MGL3), the ABL is very stable with air temperature being more than a degree warmer than the LSWT all along the track. The amplitude of the LSWT variability is significantly smaller than during summer but also much larger than during fall. It is obvious from these plots that no

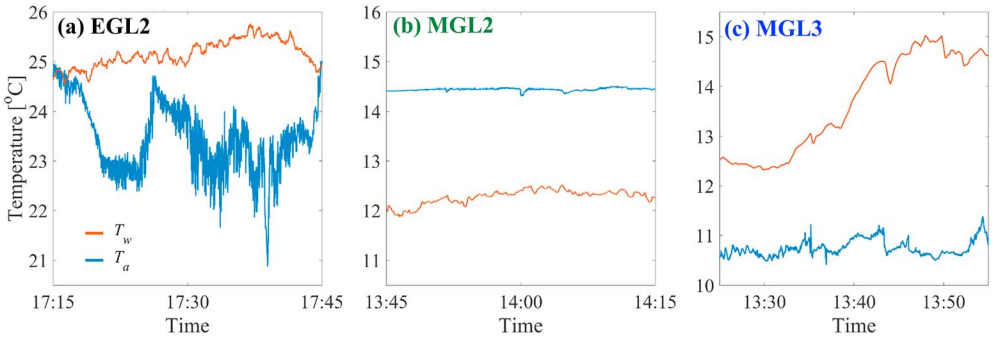

Figure 3. Time series of lake surface water temperature (LSWT; T_w, blue lines) and air temperature (T_a, orange lines) along the track of ZiviCat for three selected missions: (a) EGL2, (b) MGL2, and (c) MGL3. A 30-min duration covering the BLIMP imagery time was selected for all missions. The track is shown for each mission as a red dashed line in Figure 2. Note that the temperature range is similar in each panel (5.5 °C).

correlation can be established between the patterns of the air and the water temperatures along the tracks, as was also the case in previous studies (e.g., Assouline et al., 2008; Solcerova et al., 2018; Vercauteren et al., 2008; Q. Y. Zhang & Liu, 2013). Correlations may exist on scales smaller than the subpixel scales, which, as explained above, cannot be resolved with our equipment. When the same data are plotted as scatter plots (Figure 4), similar differences between the three missions are again evident. In summer (EGL2), the range of variability of the LSWT is dominant over that of air temperature, whereas in fall (MGL2) and in spring (MGL3), the range of variability of the air temperature is much larger than that of LSWT. In all three missions there is an apparent trend of air temperature warming over the duration of the mission. This may be due to ongoing air warming due to cloud-free skies and solar radiation being close to the maximum for that time of the year. It is evident that this warming does not affect LSWT but does influence the degree of ABL stability.

The thermal images that were collected during these missions provide LSWT maps with unprecedented resolution. The details that are visible in these maps may open up new research approaches. They may serve to refine ground truthing of satellite data that continue to progress to ever higher resolution. The spatial details and particularly the frontal gradients that are obvious in these maps may contribute to advancing the understanding of physical and biogeochemical limnological processes on smaller scales, especially the dynamics of air-water exchange. For example, the subpixel LSWT variability in lakes affects the estimates of the exchange of mass, heat, and momentum at the air-water interface (Vercauteren et al., 2008) and may impact on numerical weather prediction results (Balsamo et al., 2012; Le Moigne et al., 2016). Below, we investigate the effect of subpixel LSWT patterns on the surface cooling estimates and evaluate ABL stability conditions for the selected field missions.

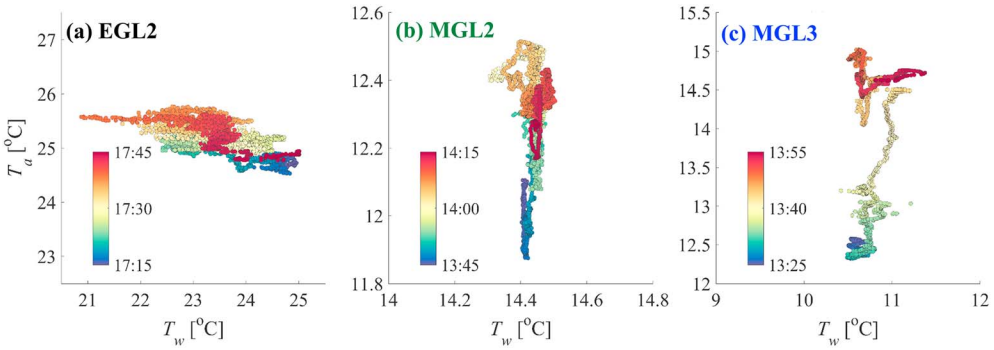

Figure 4. Measured air temperature T_a as a function of measured lake surface water temperature (T_w) for three selected missions: (a) EGL2, (b) MGL2, and (c) MGL3; same data as in Figure 3. Colors in the legend indicate the time of measurement. Note that the temperature range is different in each panel.

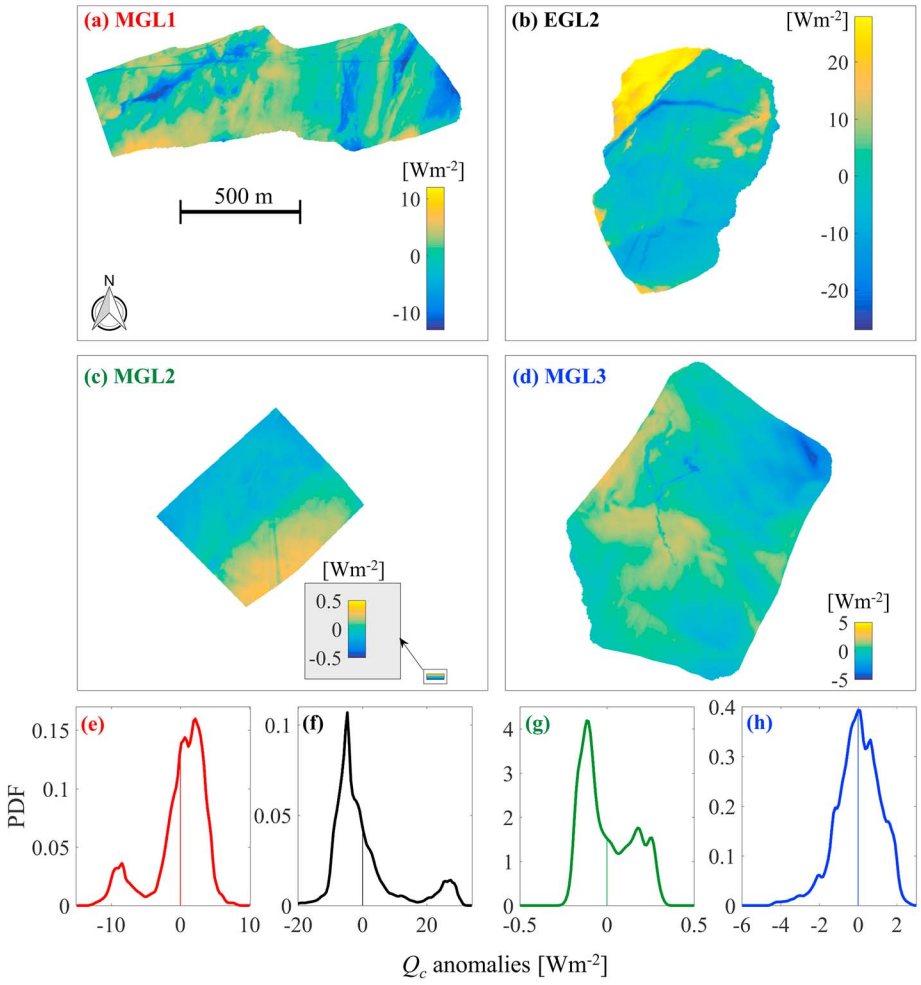

Figure 5. Same as Figure 2 but for lake surface cooling anomaly patterns. PDF = probability density function.

3.2. Subpixel-Scale Surface Cooling Patterns and Distributions

We computed lake surface cooling Q_c maps using equations 1 to (4a) and (4b), the obtained LSWT spatial patterns (Figure 2), and the area-averaged meteorological data (Table 2). We address the significance of the assumption of constant meteorological conditions on the results using a sensitivity analysis given in section 3.4. Figure 5 shows the surface cooling maps and their corresponding PDF distributions. Higher LSWT variability (Figure 2) results in greater spatial variability in surface cooling (Figure 5). The spatial variability of Q_c of MGL2 (Figure 5c) is negligible and reflects the small variability of LSWT (Figure 2c). Although the Q_c patterns are similar to the subpixel-scale LSWT structures (Figure 2), the PDF distributions (bottom panels plots in Figure 5) may be different from the LSWT PDF curves (Figure 2). This difference is more evident for the missions with higher LSWT variability, that is, MGL1 and EGL2, and at the tails of the distributions. A positive skewness (value of 1.5) is found for the Q_c distribution of EGL2 (Figure 5f), which is different from the responses to LSWT heterogeneity of MGL1 (Figure 5e) and MGL3 (Figure 5h) that have skewness values of −1.2 and −0.5, respectively.

The Q_c PDF distributions are quite different compared to the LSWT PDF distributions. This is mainly due to the nonlinearity in the turbulent heat flux formulas. More specifically, the Monin-Obukhov similarity theory depends on ABL stability (ζ) conditions, since ζ is coupled with the surface turbulent heat fluxes and surface momentum flux. The effect of this nonlinearity is higher under near-neutral conditions, that is, for small air-water temperature differences and weak surface stress (Mahrt & Hristov, 2017; Mahrt & Khelif, 2010). Therefore, investigating the ABL stability condition can be helpful when interpreting the obtained surface cooling distributions.

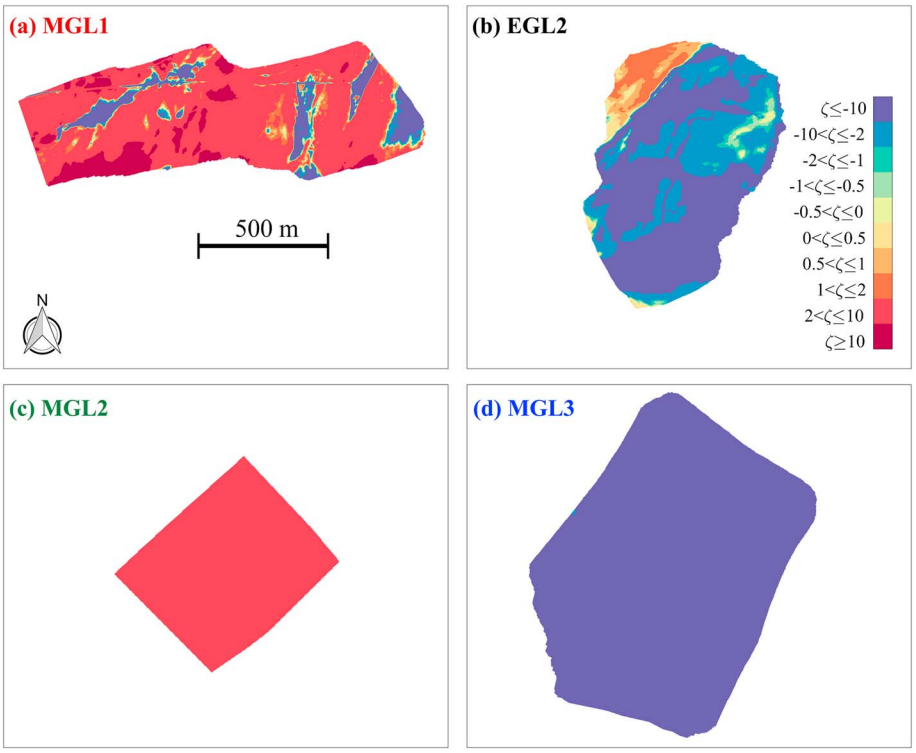

Figure 6. Atmospheric boundary layer stability patterns for the four selected field missions: (a) MGL1 (predominantly unstable), (b) EGL2 (predominantly stable), (c) MGL2 (very unstable), and (d) MGL3 (very stable). For the location and the date/season of each panel see Figure 1. Note that all panels cover an approximately 1.4-km × 1.4-km area (~2 typical satellite pixels). Colors are defined in the legend in (b).

The ABL stability conditions for the selected missions are shown in Figure 6. The atmospheric thermal boundary layer stability is defined in equations 4a and 4b (Woolway et al., 2015; Zeng et al., 1998). Our results indicate that the ABL is very unstable for the MGL2 mission (Figure 6c) and very stable for MGL3 (Figure 6d), over the entire studied areas. Most of the MGL1 ABL map (Figure 6a) is very unstable with some very stable and near-neutral regions corresponding to cold patches (Figure 2a). The ABL during EGL2 (Figure 6b) was found to be mainly very stable but with very unstable and near-neutral conditions over the warmer parts (Figure 2b). Hereinafter, we refer to the MGL1 mission as "predominantly unstable" and the EGL2 mission as "predominantly stable." Comparing the results in Figures 2, 5, and 6 indicates that for a similar LSWT range, the range of the surface cooling variation is higher under unstable (panels a) than stable ABL conditions (panels b). For example, there is more temperature variability in Figure 2b than in the surface cooling in Figure 5b in the very stable areas. Compared to Figures 2e and 2f, the tails of the PDF curves in Figures 5e and 5f also show higher PDF values for negative anomalies (corresponding to very stable conditions). A clear example is the second smaller peak formed in the left part of the PDF curve for MGL1 (Figure 5e) that does not exist in the corresponding LSWT distribution (PDF curve in Figure 2e).

The spatial variability of LSWT, and consequently surface cooling, is much higher during the MGL1 field mission in the spring (Figure 5a) than during MGL2 (Figure 5c) in the fall, even though both are on average very unstable. The net heat flux (including solar short-wave and atmospheric long-wave radiations) was positive for MGL1, whereas it was negative during the MGL2 mission (results not shown here). The net heating under weak wind conditions resulted in a strong stratification during the MGL1 mission with a vertical temperature gradient of >2.5 °C in the 1.5-m-thick surface layer (not shown here), which can enhance the water resistance to thermal mixing. In contrast, the MGL2 near-surface (1.5-m depth) temperature profiles showed an almost well-mixed layer with a vertical temperature gradient of <0.2 °C. These observations suggest that background stratification and net surface heat flux are also important for the development of the spatial LSWT pattern and consequently the spatial variability of surface cooling under very unstable conditions.

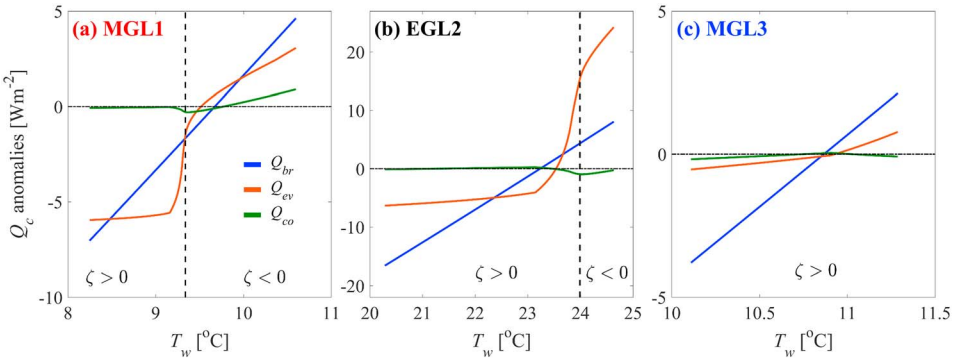

Figure 7. Anomaly variation (with respect to the mean spatial surface cooling) of back radiation Q_{br}, latent Q_{ev}, and sensible Q_{co} heat fluxes as a function of lake surface water temperature T_w, for three of the selected field missions: (a) MGL1 (predominantly unstable), (b) EGL2 (predominantly stable), and (c) MGL3 (very stable). The vertical dashed lines in (a) and (b) indicate the neutral condition, $\zeta = 0$. Colors are defined in the legend in (a).

The variation of the different surface cooling components, Q_{br}, Q_{ev}, and Q_{co}, as a function of LSWT (T_w) for the MGL1, EGL2, and MGL3 missions (Figure 7) indicates that the long-wave back radiation Q_{br} (blue lines in Figure 7) changes linearly over the measured temperature ranges. It is the controlling component during the MGL3 mission (Figure 7c) with a very stable ABL over the entire area (Figure 6d). Convective cooling Q_{co} (green lines in Figure 7) provides the smallest contribution among surface cooling terms and was comparable to the other terms only under very unstable conditions, as seen at the right end of Figure 7a. We did not show the corresponding results for the MGL2 mission because of the small variation of LSWT and Q_c.

A substantial variation of the evaporative cooling Q_{ev} was found during all the missions (brown lines in Figures 7a and 7b). The results suggest that three different types of Q_{ev} variation as a function of LSWT can be observed: (i) it is nearly flat and linear under very stable ABL conditions with negative Q_c anomalies (left part of the curves), (ii) a substantial nonlinear change is seen when going from stable to unstable ABL conditions (close to vertical dashed lines in the near-neutral zone), and (iii) a linear change with a positive slope for very unstable ABLs with positive Q_c anomalies (right part of the curves). Type (i) corresponds to the negative modes in the Q_c anomaly distributions (left part of the PDF curves in Figures 5e and 5f). For the EGL2 mission, type (i) covers a wide range of the LSWT distribution (cf. Figure 2f with 5b). The corresponding negative mode in the PDF curve of the Q_c anomaly is large (Figure 5f) with a positive skewness, whereas the LSWT PDF is negatively skewed (Figure 2f). In contrast, for the MGL1 mission, type (i) corresponds to a relatively small segment of the LSWT pattern (cf. Figure 2e with 5a). As a result, the negative PDF mode is relatively small and therefore has a negligible impact on the Q_c response to the LSWT distribution; that is, both the LSWT and Q_c anomalies show a negative PDF skewness. This variation is higher for EGL2 due to the higher wind speed during the EGL2 mission compared to MGL1 (Table 2).

3.3. Effect of Area-Averaged Surface Water Temperatures on the Surface Cooling Estimates

Our results reveal that subpixel-scale LSWT heterogeneity can be significant, in particular, under weak wind and near-neutral ABL stability conditions (Figure 2). It was also found that the surface cooling response to the LSWT under such conditions is nonlinear (Figures 5 and 7). This suggests that surface cooling, and consequently the net surface heat flux estimation at satellite pixel resolutions that do not capture these subpixel-scale LSWT variations, may be biased by the spatial averaging, as has been shown for large-scales and over open waters (Gulev, 1997; Mahrt & Khelif, 2010; Mahrt et al., 2012).

In order to investigate the significance of this averaging effect on heat flux, we compared Advanced Very High Resolution Radiometer satellite images (~1.1-km × 1.1-km pixel size) with the field data discussed above. LSWT satellite retrieval was performed following Riffler et al. (2015). A bias and root-mean-square difference within the range of −0.5 to 0.6 °C and 1.0 to 1.6 °C, respectively, were reported for satellite-based temperatures in comparison with in situ point measurements (Riffler et al., 2015). For the missions EGL2 and MGL2, satellite overpasses occurred during the field measurements and thus allow a direct comparison. The excerpts from these satellite images corresponding to the field observation areas of the present study are

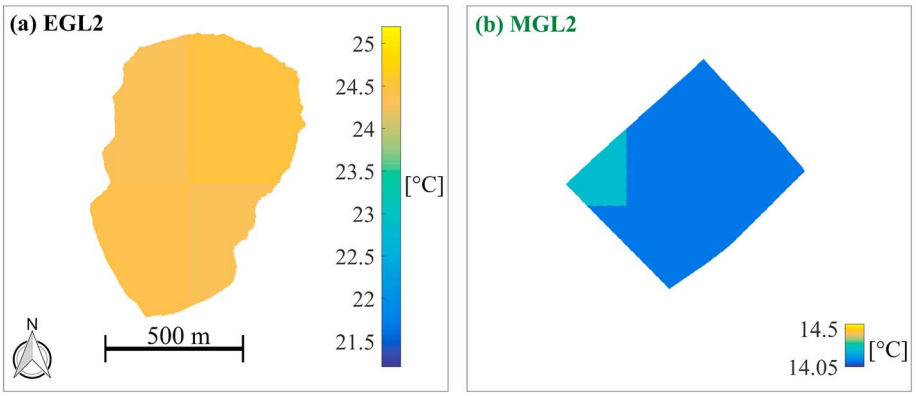

Figure 8. Lake surface water temperature maps for two of the selected missions, obtained from satellite images taken during the missions: (a) EGL2 and (b) MGL2. Areas in the maps are composed of different pixels. Note that all panels cover an approximately 1.4-km × 1.4-km area (~2 typical satellite pixels). The length of the temperature legends in the two panels is proportional to the corresponding selected surface water temperature spatial range (slightly different from Figure 2).

shown in Figure 8. Even though they are composed of parts from different pixels, satellite-derived LSWT variability in the areas is much smaller than that observed in the BLIMP maps (Figure 2). The complete satellite images of the lake surface show a greater LSWT range (Figure S2 in SI), thus indicating large-scale spatial heat flux variability. The mean LSWTs in the satellite images and the BLIMP images are similar (Table 3), confirming that the satellite image correction is reasonable.

Here, we applied the selected subpixel-scale LSWT maps obtained with our airborne remote sensing platform (Figure 2) together with the calibrated bulk formulas over Lake Geneva (equations 1 to 4a and 4b) to investigate this averaging effect for the surface area of a satellite pixel. A mean spatial filter with variable size was applied to the LSWT patterns to produce thermal maps with different spatial resolution. In this operation, each of the BLIMP pixel values was replaced with the mean (average) value of a pixel and a predefined number of neighborhood pixels. Starting from the LSWT maps at their initial resolution (given in Table 2), the filtered patterns at 20-, 100-, and 500-m resolution were estimated. The spatial filter preserves the mean spatial LSWT value in all missions for the various filter sizes. Due to the negligible spatial variability of LSWT in MGL2, the operation was not performed for this case. Figure 9a shows the resulting distributions of the LSWT anomalies with different spatial resolution compared to the mean spatial value at the initial resolution. The results demonstrate that the range of LSWT spatial variability decreases with decreasing pixel resolution. However, the difference between the distributions with 1- and 20-m resolution was found to be negligible. This indicates that the surface temperature features with an O(10 m) horizontal scale were dominant for the selected missions. By further decreasing the pixel resolution, the reduction of the 0.5–99.5 percentiles ranges (whiskers in Figure 9a) is more pronounced than the interquartile ranges (filled rectangles in Figure 9a) and is mainly attributed to the progressively disappearing cold features. The LSWT range for the 1-km filtered data is similar to that seen in the satellite images/pictures (Figure 8).

From the spatially filtered LSWT maps, the surface cooling Q_c maps at different spatial resolutions were estimated using the constant meteorological parameters given in Table 2 as in the analysis of the original maps above. Figure 9b shows the calculated distributions of the Q_c anomalies for the selected missions. The surface cooling subpixel-scale variability is higher during the EGL2 mission with a positive skewness that was discussed above. Our results, similarly to Mahrt and Hristov (2017), demonstrate that under near-neutral conditions (MGL1 and EGL2), LSWT heterogeneity is more influenced by the stably stratified parts of the ABL while the turbulent heat flux spatial variability is dominated by the unstable parts of the ABL.

The area-averaged surface cooling Q_c values were also calculated (Figure S3 in SI) for the same pixel resolutions and for the four selected

Table 3
BLIMP/Satellite (AVHRR) Mean LSWTs in Degrees Celsius for the Same Surface Areas (See Figures 2 and 8)

Date source	EGL2	MGL2
BLIMP	23.2 (0.6)	14.5 (0.01)
AVHRR	24.4	14.1

Note. The values in parentheses indicate the standard deviation. AVHRR = Advanced Very High Resolution Radiometer; LSWTs = lake surface water temperatures.

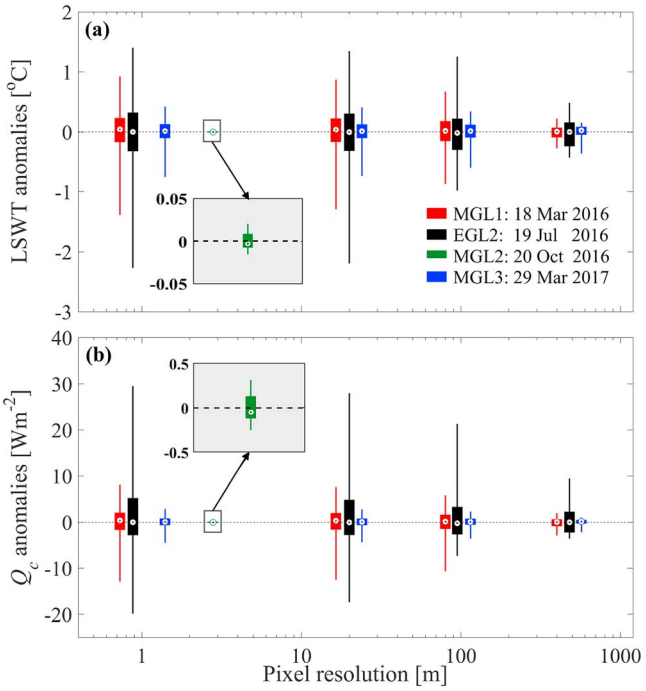

Figure 9. Box plots of anomaly distribution as a function of pixel resolution for the four selected field missions, MGL1, EGL2, MGL2, and MGL3, for (a) lake surface water temperature (LSWT), T_w, and (b) surface cooling, Q_c. The results are centered around the original O(1 m) resolution given in Table 2 and the filtered 20-, 100-, and 500-m pixel resolutions. The white circles, the filled rectangles, and the whiskers indicate the median, the interquartile range (25 to 75 percentiles), and the 0.5 to 99.5 percentiles (indicative for the total range), respectively. Note the logarithmic scale on the *x* axis. Insets: zoom of the MGL2 results at O(1 m) pixel resolution. The legend in panel (a) gives the date/season of each mission.

field missions. The results (Figure 9b) indicate that the spatial mean Q_c for the MGL1 mission (predominantly unstable) increases by ~0.5 W/m^2 from subpixel-scale O(1 m) to large-scale O(1 km) resolution (mean spatial value), while a decrease of ~3.5 W/m^2 for the same resolution range was found for EGL2 (predominantly stable). The spatial mean Q_c value also decreased but negligibly (~0.05 W/m^2) for the very stable MGL3 mission when comparing high-resolution to low-resolution patterns. These findings demonstrate that in the surface heat flux estimation of inland water bodies, the errors associated with the area-averaged LSWT are expected to be higher under near-neutral conditions (Gutowski et al., 1998; Mahrt & Hristov, 2017), a condition that is not common on an annual basis over lakes (Verburg & Antenucci, 2010; Woolway et al., 2017). In order to further investigate the effect of the above estimated biases of the calculated surface cooling induced by LSWT subpixel-scale heterogeneity on the overall heat budget of a large lake such as Lake Geneva, and in particular, in a long-term analysis, a more extensive data base would be required; this currently does not exist.

3.4. Sensitivity Analysis

The quality of the results is also affected by errors associated with the assumption of constant meteorological data, model simplifications/limitations (in particular turbulent heat flux parameterizations), and uncertainties in the ZiviCat/BLIMP measured and corrected data, for example, the difference between skin (top 10- to 500-μm layer) and near-surface temperatures (Minnett et al., 2011; Wilson et al., 2013). To quantify the uncertainty associated with the errors in meteorological parameter sampling, a sensitivity analysis on the mean meteorological parameters was performed. The results (Text S1 and Figures S4 and S5 in SI) revealed that the bias in meteorological condition sampling, particularly wind speed, can affect both the mean and the range of spatial surface cooling. The error in the air temperature may also alter the surface cooling distribution from negatively skewed to positively skewed and hence affect the area-averaged estimates. The air temperature results can approximate the uncertainty associated with the air-water temperature difference and therefore the bias in skin-bulk difference of water temperatures.

To further investigate the effect of the air temperature bias on the results of this study, a sensitivity analysis on the surface cooling estimates of EGL2, MGL2, and MGL3, for which ZiviCat air temperature data are available, was carried out. Minimum, maximum, and mean values of the measured air temperature during a 30-min window at the observation time (Figures 3 and 4) were used to obtain the PDF distribution of Q_c anomaly patterns (Figures 10 and S5 in SI). The results indicated that for MGL2 (very unstable ABL) and MGL3 (very stable ABL) the effect of bias in the air temperatures on the Q_c anomalies distribution is insignificant. However, the smaller temperature values tend to shift the ABL conditions toward unstable ABL and consequently change the Q_c anomalies distribution (Figure 10a). The interquartile range, that is, 25–75 percentile, is wider under lower air temperatures (Figure S5a in SI). However, the total range (0.5–99.5 percentile) of the Q_c anomalies variation is not significant compared to the interquartile range (Figure S5a in SI). Furthermore, the EGL2 (Figure 10a) and MGL3 (Figure 10c) results show the same skewness under different air temperature values.

In addition, we investigated the effect of turbulent heat flux parameterization by employing the commonly used formulation of Zeng et al. (1998). The results (Text S2 and Figure S6 in SI) demonstrated that the turbulent heat flux parameterization can affect the subpixel-scale surface cooling heterogeneity and therefore the area-averaged results at the satellite pixel resolution. However, the main spatial features of surface cooling predicted by the two parameterizations were similar.

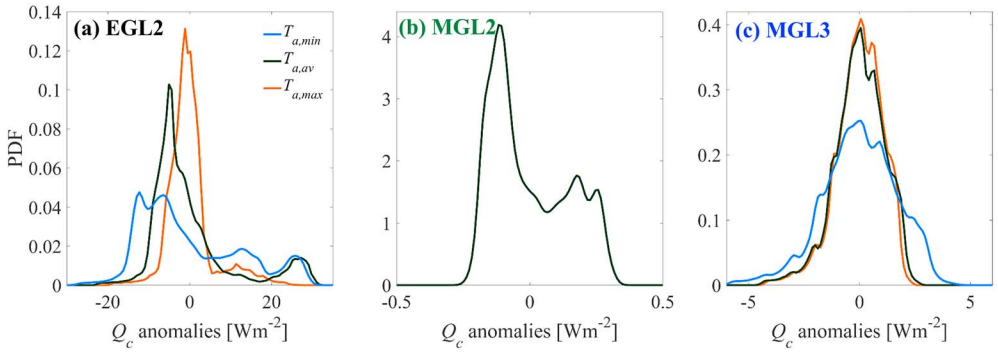

Figure 10. Probability distribution function (PDF) curves of surface cooling (Q_c) anomaly patterns under different air temperature conditions (minimum, maximum and mean values) for (a) EGL2, (b) MGL2, and (c) MGL3. For the minimum, maximum, and mean values for each mission, see the along-track measured time series (Figure 3). Note that there is a high amount of overlap between the three lines in (b). These results can be compared with those in Figure 5 where a constant air temperature was assumed.

4. Summary and Conclusions

An airborne balloon-launched remote sensing platform (BLIMP) accompanied by an autonomously operating catamaran (ZiviCat) for ground truthing was used to resolve the subpixel satellite scale O(1 m) to O(100 m) LSWT heterogeneity over Lake Geneva. Four different daytime LSWT maps covering different ABL stability conditions were selected to estimate the associated surface cooling spatial variability and the effect of area-averaged LSWT on the surface heat flux estimation at a typical satellite pixel resolution of O(1 km). The bulk aerodynamic relationship implementing Monin-Obukhov similarity was used to calculate the turbulent surface heat fluxes. The meteorological values were assumed to be constant during the short-term studied periods (less than 30 min).

The measured LSWT patterns showed a maximum spatial variation of >2 and >3.5 °C at the beginning of spring and in the middle of summer, respectively, under near-neutral ABL and weak wind conditions. The LSWT PDF distributions were negatively skewed, a PDF shape that was attributed to the cold patches and fronts in the selected patterns. Comparison of the cold season LSWT data with those at the beginning of the spring revealed that, in addition to the ABL stability, the net surface energy, surface mixing, and background stratification must be considered when investigating LSWT heterogeneity.

The corresponding calculated surface cooling patterns preserved the main subpixel-scale features of the LSWT data. However, during summer, under stable and unstable ABL conditions, the surface cooling distribution was significantly different than that of the LSWT distribution. This is related to the nonlinearity in the latent heat flux estimation under near-neutral conditions that caused the negative skewness distribution of the LSWT map to turn into a positively skewed surface cooling one. Furthermore, this suggests that using area-averaged LSWT data (not resolving the subpixel-scale heterogeneity) may result in errors in the surface cooling estimation. To address this, we applied a mean spatial filter with variable size to the LSWT patterns of the selected missions. The corresponding surface cooling distributions were then calculated. The results indicate that the heterogeneous-homogeneous differences in surface cooling estimations are greater for near-neutral conditions. Under predominantly stable conditions, the area-averaged surface cooling showed a reduction of ~3.5 W/m^2 when the heterogeneous O(1 m) subpixel-scale resolution results were compared with more homogeneous O(1 km) resolution results, typical for satellite pixel scales. For the same pixel resolution variation, the mean surface cooling estimation increased by ~0.5 W/m^2 for the predominantly unstable case. Extrapolating such subpixel-scale variability of surface cooling over the entire surface of a large inland water body, for example, Lake Geneva in our case, may significantly modify its overall heat budget analysis, when compared to one based on satellite pixel scales, especially for long-term studies.

These measurements were taken under daytime and weak wind conditions over a large inland water body. Although this study was limited to small sections of the lake surface, it provided unprecedented details and insight into the dynamics of subpixel satellite scale heterogeneity of LSWT. Further field measurement campaigns should be carried out over larger areas and a wider range of conditions, in order to confirm and

extend the present results. The measurement platforms and methodology that we developed can also be useful to study the dynamics of other processes in lakes such as the near-shore processes, for example, thermal biomes.

Acknowledgments
This work was supported by the Fondation pour l'Etude des Eaux du Léman (FEEL), Lausanne, Switzerland, EPFL (grant no. 5257, 2012–2015). Supplementary meteorological data were provided by the Federal Office of Meteorology and Climatology in Switzerland, MeteoSwiss. The BLIMP LSWT maps and ZiviCat in situ LSWT and air temperature data are available from http://doi.org/10.5281/zenodo.1470204. The authors would like to thank J.-L. Liardon, P.O. Paccaud, B. Geissmann, L. Zulliger, J. Béguin, P. Klaus, N. Gujja Shaik, S. Benketaf, K. Kangur, M. Pagnamenta, L. Hostettler, N. Bongard, G. Ulrich, B. Grossniklaus, A. Rosselet, M. Bolay, J. Rossier, Y. Poffet, and N. Roussel for their contribution to designing, testing, and improving of the BLIMP and ZiviCat platforms used in this research. We also wish to thank D. Sage, A. Ivanov, and S. Tulyakov for their help and advice on BLIMP image processing. We extend a special thanks to Htet Kyi Wynn for assisting with the fieldwork. The constructive comments and suggestions made by the reviewers that helped improve the paper were greatly appreciated.

References

Adrian, R., O'Reilly, C. M., Zagarese, H., Baines, S. B., Hessen, D. O., Keller, W., et al. (2009). Lakes as sentinels of climate change. *Limnology and Oceanography*, *54*(6part2), 2283–2297. https://doi.org/10.4319/lo.2009.54.6_part_2.2283

Alcantara, E. H., Stech, J. L., Lorenzzetti, J. A., Bonnet, M. P., Casamitjana, X., Assireu, A. T., & Novo, E. M. L. D. (2010). Remote sensing of water surface temperature and heat flux over a tropical hydroelectric reservoir. *Remote Sensing of Environment*, *114*(11), 2651–2665. https://doi.org/10.1016/j.rse.2010.06.002

Arvola, L., George, G., Livingstone, D. M., Järvinen, M., Blenckner, T., Dokulil, M. T., et al. (2010). The impact of the changing climate on the thermal characteristics of lakes. In G. George (Ed.), *The impact of climate change on European Lakes* (pp. 85–101). Dordrecht, Netherlands: Springer.

Assouline, S., Tyler, S. W., Tanny, J., Cohen, S., Bou-Zeid, E., Parlange, M. B., & Katul, G. G. (2008). Evaporation from three water bodies of different sizes and climates: Measurements and scaling analysis. *Advances in Water Resources*, *31*(1), 160–172. https://doi.org/10.1016/j.advwatres.2007.07.003

Austin, J. A., & Colman, S. M. (2007). Lake Superior summer water temperatures are increasing more rapidly than regional air temperatures: A positive ice-albedo feedback. *Geophysical Research Letters*, *34*, L06604. https://doi.org/10.1029/2006GL029021

Balsamo, G., Salgado, R., Dutra, E., Boussetta, S., Stockdale, T., & Potes, M. (2012). On the contribution of lakes in predicting near-surface temperature in a global weather forecasting model. *Tellus Series A*, *64*(1), 15829. https://doi.org/10.3402/Tellusa.V64i0.15829

Barry, D. A., Liardon, J.-L., Paccaud, P., Klaus, P., Gujja Shaik, N. S., Rahaghi, A. I., & Lemmin, U. (2019). A low-cost, autonomous mobile platform for limnological investigations, supported by high-resolution mesoscale airborne imagery. *PLoS One*. https://doi.org/10.1371/journal.pone.0210562

Bauersachs, T., Rochelmeier, J., & Schwark, L. (2015). Seasonal lake surface water temperature trends reflected by heterocyst glycolipid-based molecular thermometers. *Biogeosciences*, *12*(12), 3741–3751. https://doi.org/10.5194/bg-12-3741-2015

Beaulieu, M., Pick, F., & Gregory-Eaves, I. (2013). Nutrients and water temperature are significant predictors of cyanobacterial biomass in a 1147 lakes data set. *Limnology and Oceanography*, *58*(5), 1736–1746. https://doi.org/10.4319/lo.2013.58.5.1736

Binding, C. E., Greenberg, T. A., McCullough, G., Watson, S. B., & Page, E. (2018). An analysis of satellite-derived chlorophyll and algal bloom indices on Lake Winnipeg. *Journal of Great Lakes Research*, *44*(3), 436–446. https://doi.org/10.1016/j.jglr.2018.04.001

Bonvin, F., Razmi, A. M., Barry, D. A., & Kohn, T. (2013). Micropollutant dynamics in Vidy Bay-A coupled hydrodynamic-photolysis model to assess the spatial extent of ecotoxicological risk. *Environmental Science & Technology*, *47*(16), 9207–9216. https://doi.org/10.1021/es401294c

Brodeau, L., Barnier, B., Gulev, S. K., & Woods, C. (2017). Climatologically significant effects of some approximations in the bulk parameterizations of turbulent air-sea fluxes. *Journal of Physical Oceanography*, *47*(1), 5–28. https://doi.org/10.1175/Jpo-D-16-0169.1

Castro, S. L., Emery, W. J., Wick, G. A., & Tandy, W. (2017). Submesoscale sea surface temperature variability from UAV and satellite measurements. *Remote Sensing*, *9*(11), 1089. https://doi.org/10.3390/Rs9111089

Cimatoribus, A. A., Lemmin, U., Bouffard, D., & Barry, D. A. (2018). Nonlinear dynamics of the near-shore boundary layer of a large lake (Lake Geneva). *Journal of Geophysical Research: Oceans*, *123*(2), 1016–1031. https://doi.org/10.1002/2017JC013531

Davies, J. A., Robinson, P. J., & Nunez, M. (1971). Field determinations of surface emissivity and temperature for Lake Ontario. *Journal of Applied Meteorology*, *10*(4), 811–819. https://doi.org/10.1175/1520-0450(1971)010<0811:FDOSEA>2.0.CO;2

Fairall, C. W., Bradley, E. F., Hare, J. E., Grachev, A. A., & Edson, J. B. (2003). Bulk parameterization of air-sea fluxes: Updates and verification for the COARE algorithm. *Journal of Climate*, *16*(4), 571–591. https://doi.org/10.1175/1520-0442(2003)016<0571:Bpoasf>2.0.Co;2

Garbe, C. S., Schimpf, U., & Jahne, B. (2004). A surface renewal model to analyze infrared image sequences of the ocean surface for the study of air-sea heat and gas exchange. *Journal of Geophysical Research*, *109*, C08s15. https://doi.org/10.1029/2003JC001802

Garbe, C. S., Spies, H., & Jahne, B. (2003). Estimation of surface flow and net heat flux from infrared image sequences. *Journal of Mathematical Imaging and Vision*, *19*(3), 159–174. https://doi.org/10.1023/A:1026233919766

Gulev, S. K. (1997). Climatologically significant effects of space-time averaging in the North Atlantic sea-air heat flux fields. *Journal of Climate*, *10*(11), 2743–2763. https://doi.org/10.1175/1520-0442(1997)010<2743:Cseost>2.0.Co;2

Gutowski, W. J., Otles, Z., & Chen, Y. B. (1998). Effect of ocean surface heterogeneity on climate simulation. *Monthly Weather Review*, *126*(6), 1419–1429. https://doi.org/10.1175/1520-0493(1998)126<1419:Eoosho>2.0.Co;2

Handler, R. A., & Smith, G. B. (2011). Statistics of the temperature and its derivatives at the surface of a wind-driven air-water interface. *Journal of Geophysical Research*, *116*, C06021. https://doi.org/10.1029/2010JC006496

Hsu, S. A., Meindl, E. A., & Gilhousen, D. B. (1994). Determining the power-law wind-profile exponent under near-neutral stability conditions at sea. *Journal of Applied Meteorology*, *33*(6), 757–765. https://doi.org/10.1175/1520-0450(1994)033<0757:Dtplwp>2.0.Co;2

Hughes, P. J., Bourassa, M. A., Rolph, J. J., & Smith, S. R. (2012). Averaging-related biases in monthly latent heat fluxes. *Journal of Atmospheric and Oceanic Technology*, *29*(7), 974–986. https://doi.org/10.1175/Jtech-D-11-00184.1

Le Moigne, P., Colin, J., & Decharme, B. (2016). Impact of lake surface temperatures simulated by the FLake scheme in the CNRM-CM5 climate model. *Tellus Series A*, *68*(1), 31274. https://doi.org/10.3402/Tellusa.V68.31274

Lemmin, U., & Amouroux, A. (2013). The influence of climate change on Lake Geneva. In C. R. Goldman, M. Kumagai, & R. D. Robarts (Eds.), *Climatic change and global warming of inland waters* (pp. 201–217). Chichester, UK: John Wiley. https://doi.org/10.1002/9781118470596.ch12

Liardon, J.-L., & Barry, D. A. (2017). Adaptable imaging package for remote vehicles. *HardwareX*, *2*, 1–12. https://doi.org/10.1016/j.ohx.2017.04.001

Liardon, J.-L., Hostettler, L., Zulliger, L., Kangur, K., Shaik, N. G., & Barry, D. A. (2017). Lake imaging and monitoring aerial drone. *HardwareX*, *3*, 146–159. https://doi.org/10.1016/j.ohx.2017.10.003

Lofgren, B. M., & Zhu, Y. C. (2000). Surface energy fluxes on the Great Lakes based on satellite-observed surface temperatures 1992 to 1995. *Journal of Great Lakes Research*, *26*(3), 305–314. https://doi.org/10.1016/S0380-1330(00)70694-0

Mahrt, L., & Hristov, T. (2017). Is the influence of stability on the sea surface seat flux important? *Journal of Physical Oceanography*, *47*(3), 689–699. https://doi.org/10.1175/Jpo-D-16-0228.1

Mahrt, L., & Khelif, D. (2010). Heat fluxes over weak SST heterogeneity. *Journal of Geophysical Research*, *115*, D11103. https://doi.org/10.1029/2009JD013161

Mahrt, L., Vickers, D., Andreas, E. L., & Khelif, D. (2012). Sensible heat flux in near-neutral conditions over the sea. *Journal of Physical Oceanography*, *42*(7), 1134–1142. https://doi.org/10.1175/Jpo-D-11-0186.1

Marruedo Arricibita, A. I., Dugdale, S. J., Krause, S., Hannah, D. M., & Lewandowski, J. (2018). Thermal infrared imaging for the detection of relatively warm lacustrine groundwater discharge at the surface of freshwater bodies. *Journal of Hydrology*, *562*, 281–289. https://doi.org/10.1016/j.jhydrol.2018.05.004

Minnett, P. J., Smith, M., & Ward, B. (2011). Measurements of the oceanic thermal skin effect. *Deep-Sea Res. Part II.*, *58*(6), 861–868. https://doi.org/10.1016/j.dsr2.2010.10.024

Monin, A. S., & Obukhov, A. M. (1954). Basic laws of turbulent mixing in the ground layer of the atmosphere. *Tr. Akad. Nauk SSSR Geofiz. Inst.*, *24*(151), 163–187.

Moukomla, S., & Blanken, P. D. (2017). The estimation of the North American Great Lakes turbulent fluxes using satellite remote sensing and MERRA reanalysis data. *Remote Sensing*, *9*(2), 141. https://doi.org/10.3390/Rs9020141

Nordbo, A., Launiainen, S., Mammarella, I., Lepparanta, M., Huotari, J., Ojala, A., & Vesala, T. (2011). Long-term energy flux measurements and energy balance over a small boreal lake using eddy covariance technique. *Journal of Geophysical Research*, *116*, D02119. https://doi.org/10.1029/2010JD014542

Oesch, D., Jaquet, J. M., Klaus, R., & Schenker, P. (2008). Multi-scale thermal pattern monitoring of a large lake (Lake Geneva) using a multi-sensor approach. *International Journal of Remote Sensing*, *29*(20), 5785–5808. https://doi.org/10.1080/01431160802132786

O'Reilly, C. M., Sharma, S., Gray, D. K., Hampton, S. E., Read, J. S., Rowley, R. J., et al. (2015). Rapid and highly variable warming of lake surface waters around the globe. *Geophysical Research Letters*, *42*, 10,773–10,781. https://doi.org/10.1002/2015GL066235

Paccaud, P., & Barry, D. A. (2018). Obstacle detection for lake-deployed autonomous surface vehicles using RGB imagery. *PLoS One*, *13*(10), e0205319. https://doi.org/10.1371/journal.pone.0205319

Pareeth, S., Bresciani, M., Buzzi, F., Leoni, B., Lepori, F., Ludovisi, A., Morabito, G., et al. (2017). Warming trends of perialpine lakes from homogenised time series of historical satellite and in-situ data. *Science of the Total Environment*, *578*, 417–426. https://doi.org/10.1016/j.scitotenv.2016.10.199

Rahaghi, A. I., Lemmin, U., Cimatoribus, A., Bouffard, D., Riffler, M., Wunderle, S., & Barry, D. A. (2018). Improving surface heat flux estimation for a large lake through model optimization and two-point calibration: The case of Lake Geneva. *Limnology and Oceanography: Methods*, *16*(9), 576–593. https://doi.org/10.1002/lom3.10267

Rahaghi, A. I., Lemmin, U., Sage, D., & Barry, D. A. (2019). Achieving high resolution thermal imagery in low-contrast lake surface waters by aerial remote sensing and image registration. *Remote Sensing of Environment*, *221*, 773–783. https://doi.org/10.1016/j.rse.2018.12.018

Riffler, M., Lieberherr, G., & Wunderle, S. (2015). Lake surface water temperatures of European Alpine lakes (1989–2013) based on the Advanced Very High Resolution Radiometer (AVHRR) 1 km data set. *Earth System Science Data*, *7*(1), 1–17. https://doi.org/10.5194/essd-7-1-2015

Schnieders, J., Garbe, C. S., Peirson, W. L., Smith, G. B., & Zappa, C. J. (2013). Analyzing the footprints of near-surface aqueous turbulence: An image processing-based approach. *Journal of Geophysical Research: Oceans*, *118*, 1272–1286. https://doi.org/10.1002/jgrc.20102

Sima, S., Ahmadalipour, A., & Tajrishy, M. (2013). Mapping surface temperature in a hyper-saline lake and investigating the effect of temperature distribution on the lake evaporation. *Remote Sensing of Environment*, *136*, 374–385. https://doi.org/10.1016/j.rse.2013.05.014

Solcerova, A., van Emmerik, T., van de Ven, F., Selker, J., & van de Giesen, N. (2018). Skin effect of fresh water measured using distributed temperature sensing. *Water-Sui*, *10*(2), 214. https://doi.org/10.3390/W10020214

Spence, C., Blanken, P. D., Hedstrom, N., Fortin, V., & Wilson, H. (2011). Evaporation from Lake Superior: 2—Spatial distribution and variability. *Journal of Great Lakes Research*, *37*(4), 717–724. https://doi.org/10.1016/j.jglr.2011.08.013

Van Emmerik, T. H. M., Rimmer, A., Lechinsky, Y., Wenker, K. J. R., Nussboim, S., & van de Giesen, N. C. (2013). Measuring heat balance residual at lake surface using distributed temperature sensing. *Limnology and Oceanography: Methods*, *11*(2), 79–90. https://doi.org/10.4319/lom.2013.11.79

Verburg, P., & Antenucci, J. P. (2010). Persistent unstable atmospheric boundary layer enhances sensible and latent heat loss in a tropical great lake: Lake Tanganyika. *Journal of Geophysical Research*, *115*, D11109. https://doi.org/10.1029/2009JD012839

Vercauteren, N., Bou-Zeid, E., Parlange, M. B., Lemmin, U., Huwald, H., Selker, J., & Meneveau, C. (2008). Subgrid-scale dynamics of water vapour, heat, and momentum over a lake. *Boundary-Layer Meteorology*, *128*(2), 205–228. https://doi.org/10.1007/s10546-008-9287-9

Veron, F., Melville, W. K., & Lenain, L. (2008). Infrared techniques for measuring ocean surface processes. *Journal of Atmospheric and Oceanic Technology*, *25*(2), 307–326. https://doi.org/10.1175/2007JTECH0524.1

Wilson, R. C., Hook, S. J., Schneider, P., & Schladow, S. G. (2013). Skin and bulk temperature difference at Lake Tahoe: A case study on lake skin effect. *Journal of Geophysical Research: Atmospheres*, *118*, 10,332–10,346. https://doi.org/10.1002/Jgrd.50786

Woolway, R. I., Jones, I. D., Hamilton, D. P., Maberly, S. C., Muraoka, K., Read, J. S., et al. (2015). Automated calculation of surface energy fluxes with high-frequency lake buoy data. *Environmental Modelling and Software*, *70*, 191–198. https://doi.org/10.1016/j.envsoft.2015.04.013

Woolway, R. I., & Merchant, C. J. (2018). Intralake heterogeneity of thermal responses to climate change: A study of large Northern Hemisphere lakes. *Journal of Geophysical Research: Atmospheres*, *123*, 3087–3098. https://doi.org/10.1002/2017JD027661

Woolway, R. I., Verburg, P., Lenters, J. D., Merchant, C. J., Hamilton, D. P., Brookes, J., et al. (2018). Geographic and temporal variations in turbulent heat loss from lakes: A global analysis across 45 lakes. *Limnology and Oceanography*, *63*(6), 2436–2449. https://doi.org/10.1002/lno.10950

Woolway, R. I., Verburg, P., Merchant, C. J., Lenters, J. D., Hamilton, D. P., Brookes, J., et al. (2017). Latitude and lake size are important predictors of over-lake atmospheric stability. *Geophysical Research Letters*, *44*, 8875–8883. https://doi.org/10.1002/2017GL073941

Xue, P. F., Schwab, D. J., & Hu, S. (2015). An investigation of the thermal response to meteorological forcing in a hydrodynamic model of Lake Superior. *Journal of Geophysical Research: Oceans*, *120*, 5233–5253. https://doi.org/10.1002/2015JC010740

Zeng, X. B., Zhao, M., & Dickinson, R. E. (1998). Intercomparison of bulk aerodynamic algorithms for the computation of sea surface fluxes using TOGA COARE and TAO data. *Journal of Climate*, *11*(10), 2628–2644. https://doi.org/10.1175/1520-0442(1998)011<2628:Iobaaf>2.0.Co;2

Zhang, G. Q., Yao, T. D., Xie, H. J., Qin, J., Ye, Q. H., Dai, Y. F., & Guo, R. F. (2014). Estimating surface temperature changes of lakes in the Tibetan Plateau using MODIS LST data. *Journal of Geophysical Research: Atmospheres*, *119*, 8552–8567. https://doi.org/10.1002/2014JD021615

Zhang, Q. Y., & Liu, H. P. (2013). Interannual variability in the surface energy budget and evaporation over a large southern inland water in the United States. *Journal of Geophysical Research: Atmospheres*, *118*, 4290–4302. https://doi.org/10.1002/jgrd.50435